3
Detrimental Effect of Dust Deposition

There is a serious challenge while operating an open volumetric air receiver (OVAR) in arid desert region viz. dust deposition. The OVARs comprising of porous absorbers are exposed to dust laden air and are prone to the dust deposition, as explained in Chapter 2. The deposited dust may block these pores partially or even completely. The thermal conductivity of dust particles is of the order of 2 W/mK and that of porous absorber material is about 100 - 150 W/mK. The deposited dust, therefore, forms a so-called insulating layer that prevents the heat transfer from absorber material to air. Consequently, the generated hot spots in an absorber may even lead to failure of such a system [Agrafiotis *et al.*, 2007; Schmücker, 2012]. In porous receivers, the volumetric effect is desired to minimize the radiation based heat-loss, which is non-trivial in a real scenario [Ho, 2017]. Along with these parameters, the heat flux distribution also affects the temperature distribution in an absorber (see e.g. Kasaeian *et al.*, 2017; Wang *et al.*, 2013). Gomez-Garcia *et al.* (2016) used two radiative sources viz. concentrating and diffused, and concluded that the monolithic honeycomb structure restricts the volumetric effect. A similar effect was reported by Fend *et al.* (2013) in which a single channel model was used. Numerical analysis with an innovative volumetric receiver suggested achieving the volumetric effect [Capuano *et al.*, 2015]. Cagnoli *et al.* (2017) reported the uniformity of heat flux distribution inside the pores depending on the angle of incidence onto the receiver aperture. They showed that the performance of such receivers is practically independent of the tilt angle in the range 43 - 63º and the volumetric effect was achieved at a low wind speed. In this chapter, the detrimental effect of dust deposition under volumetric and non-volumetric heat flux distribution on the heat transfer in an absorber pore is analyzed. As a next step, the performed experiments demonstrating dust deposition in an absorber pore is presented.

3.1 DUST DEPOSITION: EXPERIMENTS

Experiments are performed to demonstrate the wind driven dust deposition in a porous absorber, which is expected on-the-field condition. A preliminary outdoor experiment at a wind speed of 7.5 m/s has revealed that the straight circular absorber pores of 2 mm diameter and of 25.4 mm length may be blocked by deposited dust in about 10 minutes. In order to obtain a better insight to the dust deposition in absorber pores under a controlled condition, laboratory experiments are performed. The experimental set-up is shown in Figure 3.1(a) in which a blower is connected to a circular tube. A porous absorber is placed at the center of outlet of the circular tube. Close to the absorber, a funnel is placed for introducing sand from outside and is blown to the porous absorber in order to demonstrate the deposition of dust in the absorber pores. A cyclone separator is connected downstream of the absorber wherein a suction may be applied at its outlet for the absorber cleaning and collection of the removed dust. However, in the presented experiment, to demonstrate the deposition of dust, the suction is not applied. This is in accordance with the objective of the performed experiment. The employed experimental conditions and the sizes of dust are presented in Table 3.1.
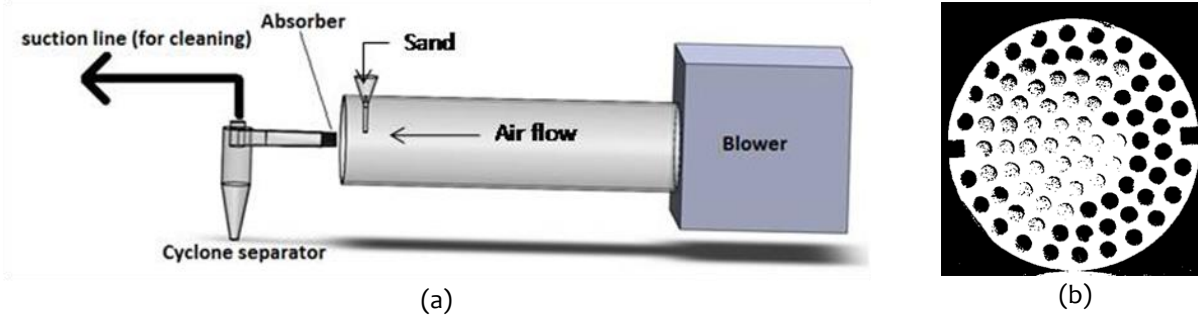
Figure 3.1: (a) Schematic of dust deposition experiment; (b) Photograph of dust deposited in absorber.

The performed experiments clearly demonstrate that the pores may be partly/fully blocked, which is evident from the black (clean) and white (blocked) image of pores in Figure 3.1(b). In the performed experiments the rate of injection of the smaller dust size is 5 times lower than that of larger dust size. From the required experimental time and the rate of injection of dust it is inferred that the larger dust sizes will block the pores even earlier than that of smaller dust sizes. These are summarized in Table 3.1 in which the rate and percentage of deposition at a particular speed of air is presented. Here the dust size is based on the American Society of Testing and Materials (ASTM) standard as shown in this table. To analyze the effect of dust deposition on heat transfer in absorber pore, heat transfer analysis is performed as described in the next sub-section.

Table 3.1: Experimental condition and outcome of dust deposition on porous absorber.

S.no.	Air speed (m/s)	Dust particle size range (µm)	ASTM number	Weight of dust taken(g)	Experiment duration (seconds)	Dust injection rate (g/s)	Deposited dust (g)	Blocked (%)
1	5.9	75-106	200	100	65	1.54	~ 2	~21
2	5.9	<53	270	60	196	0.31		

3.2 DUST DEPOSITION: HEAT TRANSFER

In the foregoing analysis it is assumed that all the pores are identical and are exposed to the same heat flux distribution in an absorber. Thus, a single circular straight pore with and without dust layer is used for analyzing the heat transfer deterioration using the two and three - dimensional numerical simulations depending on the considered absorber geometries. Analysis with a clean pore is straight forward. For the partial blockage of a pore, the two possible scenarios are (i) a dust layer is initially deposited on the pore and, subsequently, it is exposed to radiation and, (ii) a pore is already exposed to radiation and suddenly the dust deposits on its surface. The second scenario is considered being more relevant during an instantaneous sand/dust-storm. Furthermore, it is assumed that a prolonged exposure of the concentrated solar irradiance (CSI), under such a condition during operation, will lead to an eventual steady-state. The variation of thermal properties of air is considered in these simulations with the circular and square shaped straight pore based absorbers. For the circular pore a two-dimensional axi-symmetric model is selected whereas for the square channel a three-dimensional model of a pore is preferred for the obvious reasons. These are presented in the subsequent sections.

3.2.1 Two-dimensional Model: Circular Straight Channel

In this section, the effect of dust deposition and heat flux distribution in an absorber pore are illustrated. One question remains is whether this study is practically relevant or not?

As a preliminary assessment the thermal resistance offered by an additional layer of the deposited dust and its consequence is analyzed as follows:

3.2.1.1 Thermal Resistance

The deposition of dust will enhance the thermal resistance to heat transfer in an absorber pore and as a consequence the temperature difference between the absorber material (brass) and fluid (air) will be higher than that of a clean pore. The thermal resistance between absorber material and air for a clean and partially blocked pore can be easily estimated as follows:

$$
\left.
\begin{aligned}
R_{th\_cl} &= \frac{1}{h_{cl} A_{ps\_cl}} \\
R_{th\_bl} &= \frac{1}{h_{bl} A_{ps\_bl}} + \frac{\ln\left(d_{cl}/d_{bl}\right)}{2\pi k_d L}
\end{aligned}
\right\}
\tag{3.1}
$$

where, R_{th} is the thermal resistance in the pore, h is the convective heat transfer coefficient in the pore, A_{ps} is the wetted surface area of the pore, d is the hydraulic diameter of the pore, the subscripts cl and bl stands for clean and blocked pores, L is the length of the circular straight pore and, k_d is the thermal conductivity of dust. In eq. (3.1) the offered conductive resistance by the absorber material is ignored basing on its high thermal conductivity (~ 100 W/mK) in comparison to that of dust (~ 1-2 W/mK). The porosity (ε) of absorber in terms of dust layer thickness can be obtained as

$$
\varepsilon = \frac{A_c \times n_c + A_b \times n_b}{A_{cs}}, \text{where } A_c = \frac{\pi d_{cl}^2}{4} \text{ and } A_b = \frac{\pi(d_{cl} - 2t_d)^2}{4}
\tag{3.2}
$$

where, A_c is the cross section area of a clean pore, A_b is the flow cross section area of a partially blocked pore, t_d is the thickness of dust layer, n_b is the number of partially blocked pores, n_c is the number of clean pores and A_{cs} is the cross section area of absorber. Therefore, if dust deposits then the porosity of absorber will be lower than that of a clean pore. This will offer a higher resistance to the airflow and heat transfer for a given suction. For a simple analysis the uniform layer of deposited dust along the pore length is assumed. Because of the identical geometry only one pore will suffice to estimate its effect on the heat transfer. This is manifested as the rise of mean temperature difference between absorber material and air with thickness of dust layer as summarized in Table 3.2. The digits are rounded off to the first decimal point. In these calculations an average convective heat transfer coefficient is used, which ideally should vary along the length. Thus, the numbers are only representative in nature. Table 3.2 confirms that the mean temperature difference between absorber material and air will increase with the dust layer thickness as a result of the enhanced conductive resistance and decrease with Re_p as a consequence of heat transfer coefficient for a given thickness of dust layer. Thus the need for a more detailed analysis is realized. As a next step, a two-dimensional analysis is performed using ANSYS-FLUENT 13.0.

Table 3.2: Mean temperature difference between absorber material and air in a partly blocked pore with a uniform dust layer thickness.

Re_p	Dust layer thickness (Porosity in %)		
	100 μm (42%)	200 μm (33%)	300 μm (25%)
100	103.5 K	104.7 K	106.3 K
200	92.8 K	94.8 K	97.2 K
300	84.7 K	87.1 K	89.8 K

3.2.1.2 Heat Flux distribution

To understand the deterioration of heat transfer due to the deposition of dust, the steady-state investigations are performed using (a) volumetric heating or a uniform heat flux [Sharma *et al.*, 2015a,b] and (b) a realistic non-uniform heat flux distribution on the absorber material as illustrated in Figure 3.2(a) and (b). Indeed, the unsteady simulations will be preferred to estimate the required time to achieve the highest temperature.
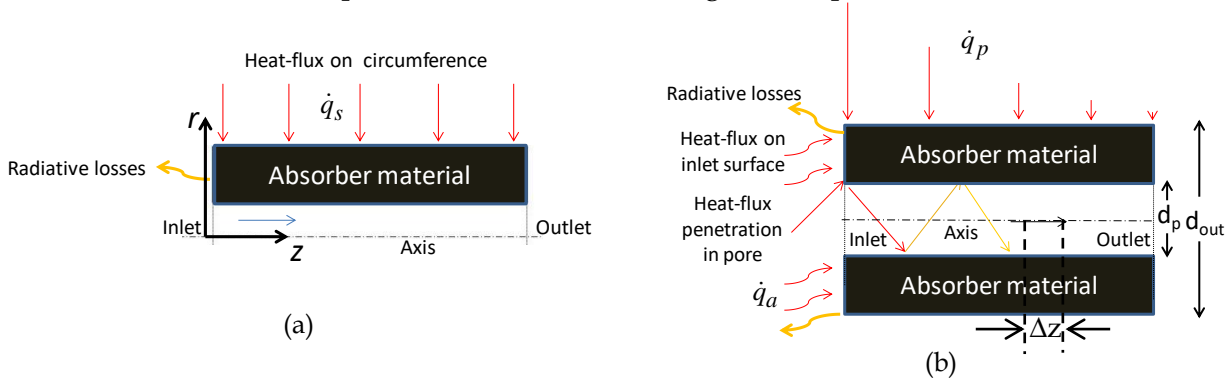

Figure 3.2: Heat flux distribution on the absorber material viz. (a) the uniform and (b) non-uniform.

An OVAR is generally tilted at an angle to face the heliostat field and thus, a part of the CSI incidents on the inlet surface of absorber metal and the rest enters in the pores. The later undergoes multiple reflections and is absorbed throughout the length of the pore as indicated in Figure 3.2(b). These figures show an axis-symmetry view of the circular pore with surrounding absorber material for the two-dimensional numerical analysis. This represents either a clean or a partly blocked condition, as the case may be. Application of a uniform heat flux as boundary condition is straightforward. However, for a non-uniform heat flux (I), the distribution as in eq. (3.3) is implemented in FLUENT with the help of user-defined function (UDF). The extinction coefficient (ξ) is adopted from the foam-type absorber [Wu *et al.*, 2011] as follows:

$$\left. \begin{aligned} I(z) &= I_0 e^{-\xi z} \\ \xi &= \frac{3(1-\varepsilon)}{d_{pore}} \end{aligned} \right\} \tag{3.3}$$

where, d_{pore} is the hydraulic diameter of a pore. A part of the CSI (q_s'') to OVAR aperture is incident on the front surface of absorber material around the pore and the rest enters the pore through the opening, which is absorbed throughout its length as depicted in Figure 3.2(b). The single pore model assumes an equal distribution of the absorber material around all the pores and thus the equivalent power balance in a pore is given by

$$\left. \begin{aligned} &\underbrace{\dot{q}_s} && = && \underbrace{\dot{q}_a} && + && \underbrace{\dot{q}_p} \\ &\text{total incident power on the single} && && \text{incident power on the} && && \text{incident power on the inner surface} \\ &\text{pore surrounded by absorber material} && && \text{absorber material of the pore} && && \text{of the pore through the opening} \\ \\ &\text{with,} \\ \\ &q_s'' = \frac{\dot{q}_s}{\left(\frac{\pi}{4} d_{out}^2\right)}, \dot{q}_a = (1-\varepsilon)q_s''\left(\frac{\pi d_{out}^2}{4}\right) \text{ and } \dot{q}_p = \varepsilon q_s''.\left(\frac{\pi d_{out}^2}{4}\right) \end{aligned} \right\} \tag{3.4}$$

Here, d_{out} is the outer diameter of the pore and the porosity defined as

$$\varepsilon = \frac{\text{Cross section (circular) area of the pore opening}}{\text{Total cross section (circular)area of the pore and surrounding absorber material}} = \frac{\pi d_{pore}^2}{\pi d_{out}^2}$$

$$\Rightarrow \frac{d_{pore}}{d_{out}} = \sqrt{\varepsilon} \tag{3.5}$$

The incident total power on the inner surface of pore (see Figure 3.2(b)) is calculated using the non-uniform heat flux distribution as in eq. (3.3), which is given by

$$\dot{q}_p = \int_0^L I_0 e^{-\xi z} \pi d_{pore}\, dz$$

$$\Rightarrow I_0 = \frac{q_s^{''} d_{pore} \xi}{4\left(1 - e^{-\xi L}\right)}\ , \tag{3.6}$$

which is used for obtaining $I(z) = I_o e^{-\xi z}$, with $I(z)$ as the heat flux distribution on the inner surface of pore. Because the analysis deals with a single pore the same $\dot{q}_p$ is adopted on its outer circumference, satisfying the conservation of energy (eq. (3.4)), to analyze the effect of heat transfer deterioration with the dust deposition as depicted in Figure 3.2(b). The resulting heat flux distribution on the outer surface of pore with absorber material, along the axial direction, is obtained by a local power balance over a representative elementary length Δz as

$$\dot{q}_p(z) = \underbrace{\left(\pi d_{pore}\Delta z\right)I(z)|_{inner\ surface}}_{Incident\ power\ on\ the\ inner\ surface} = \underbrace{\left(\pi d_{out}\Delta z\right)I(z)|_{outer\ surface}}_{Equivalent\ power\ on\ the\ outer\ (circumference)surface}$$

$$\Rightarrow I(z)|_{outer\ surface} = \left(\frac{d_{pore}}{d_{out}}\right)I(z)|_{inner\ surface}$$

The above equation ensures (a) conservation of the total input power by radiation on the pore with absorber material and (b) provide an equivalent heat flux on the outer (circumference) of pore with absorber material. The obtained $I(z)$ at the outer surface is employed as a boundary condition and is explained in Table 3.4. The non-uniform heat flux on the outer (circumference) surface is depicted by arrows of variable length.

Using eq. (3.5) results in

$$\Rightarrow I(z)|_{outer\ surface} = \sqrt{\epsilon}I(z)|_{inner\ surface}$$

Using the definition of I(z) from eq. (3.3) we obtain

$$I(z)|_{outer\ surface} = \sqrt{\epsilon}I_o e^{-\xi z} \tag{3.7}$$

Using eq. (3.6) in eq. (3.7) results in

$$I(z)|_{outer\ surface} = \sqrt{\epsilon}\frac{q_s^{''} d_{pore} \xi}{4\left(1 - e^{-\xi L}\right)}e^{-\xi z} \tag{3.8}$$

This expression of heat flux distribution along the pore length or the axial-direction (z) is implemented as a UDF for analysis.

3.2.1.3 CFD Analysis: Clean and Partly Blocked Pore

Assuming that all the pores are identical and exposed to the same condition suffices modeling a single pore. For the heat transfer analysis at the steady-state, a single pore surrounded by an absorber material is considered (see Figure 3.2). The modeled single pore geometry comprises a fluid (air) domain with temperature dependent properties and a solid (brass) domain with constant thermo-physical properties for a clean pore. For a partly blocked pore a dust layer having thickness of 100 μm/200 μm is introduced as a solid domain with thermo-physical properties of sand. This is sandwiched between the absorber and fluid domain as illustrated in Figure 3.3(a). Thus the dust-air and dust-solid interface is suitably modeled with consistent thermal boundary condition. Obviously, no such dust-layer is included in the simulations with a clean pore; see Figure 3.3(a). In an ideal situation, a uniform thickness of the deposited dust layer is expected. However, in a realistic condition, dust deposition will be generally non-uniform. To simulate these different scenarios, both the uniform dust layer (UDL) and the non-uniform dust layer (NDL) distributions along the pore length are assumed as in Figure 3.3(a). For NDL, the prescribed maximum thickness (100 μm or 200 μm) at the inlet and reduces to zero at the outlet. Moreover, both the ideal volumetric and a realistic non-uniform heating are simulated with a uniform and a non-uniform heat flux distribution on the outer circumference of pore.
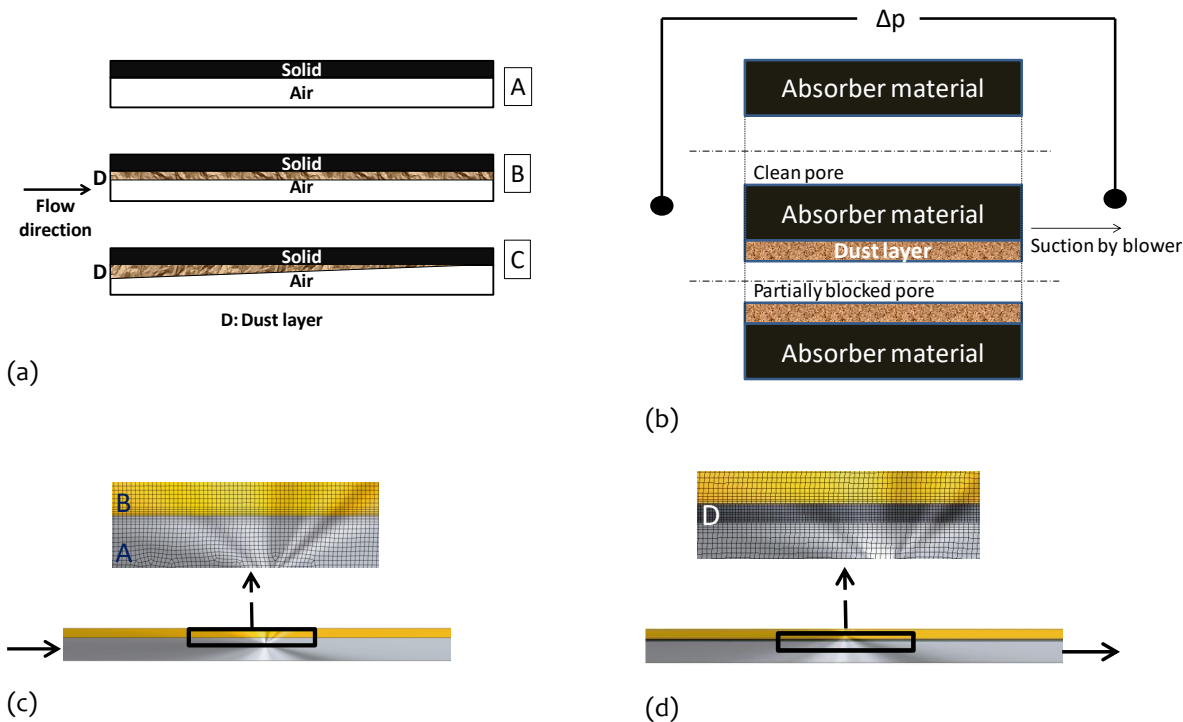

(a)

(b)

(c)

(d)

Figure 3.3: (a) Geometries of A: clean pore, B: pore with uniform dust layer (UDL), C: pore with non-uniform dust layer, (b) A schematic showing the same pressure-drop across all absorber pores due to suction (c) Employed mesh for the clean and (d) partially blocked pore (A: air, B: brass and D: dust).

Each absorber pore is subject to the same Δp inferring the applied same suction. This reflects the use of a common blower for suction through a receiver comprise of several porous absorbers. The same is depicted with a schematic of a clean and a partly blocked pore in Figure 3.3(b). In the two-dimensional simulation, a total pressure of 15.8 Pa corresponding to a $\dot{q}/\dot{m}_a \sim$ 200 kJ/kg at a power ($\dot{q}$) of 1.03 W is employed as the inlet boundary condition. Zero gage pressure is applied at the outlet. Thus the flow inside a clean and a partly blocked pore is driven by the same pressure-drop as in an absorber. The generated structured mesh in the fluid (air), the dust (sand) and the absorber material (brass) domain is shown in Figure 3.3(c) and (d). The utilized numerical setup is described in Table 3.3. The governing equations for the fluid and solid domain are as follows:

Fluid (air)

$$\nabla \cdot \vec{V} = 0$$

$$(\vec{V} \cdot \nabla)\, \vec{V} = -\frac{\nabla p}{\rho_f} + v_f\, \nabla^2\, \vec{V}$$

$$\left(\nabla \cdot \rho_f\, \vec{V} H_f\right) = \nabla \cdot \left(\frac{k_f}{c_{pf}} \nabla H_f\right)$$

Solid (absorber material/dust)

$$\nabla \cdot (k_s \nabla T) = 0$$

$$(3.9)$$

where, c_{pf} is the specific heat capacity at constant pressure of air, $\vec{V}$ is the velocity, p is the pressure, ρ_f is the density of air, k_f / k_s is the thermal conductivity of air/solid, H_f is the total enthalpy of air, T is the temperature of solid (brass/dust) and v_f is the kinematic viscosity of air. The eq. (3.9) assumes the constant properties of solid (brass/dust) and the temperature dependent properties of the fluid (air). The employed boundary conditions for the single pore model are summarized in Table 3.4 for the uniform and the non-uniform heat flux distributions, respectively. The uniform heat flux is applied only on the circumferential area of brass as in an experiment. Whereas the non-uniform heat flux is distributed on the circumference along the length and on the inlet surface of brass. For the dust layer, the boundary condition is internally computed at the solid/solid and solid/fluid interfaces as a part of consistency.

Table 3.3: Setup for the steady-state heat transfer analysis of a single pore surrounded by brass.

Mesh-type	Mesh-size (in mm)	Mesh-quality	Governing Equations	Numerical Scheme	Convergence
Structured	0.015mm - 0.05mm	Orthogonality: 0.8 to 0.99 Aspect Ratio: 5.5-7.5	Continuity, Momentum, Energy	First-order Upwind with SIMPLE algorithm	10^{-6}

The radiation based heat loss at the inlet surface of the pore is implemented using UDF as a boundary condition and the convective heat loss is ignored. The boundary conditions are also depicted using Figure 3.2 and are summarized in Table 3.4. In the depicted boundary conditions, q''_{net} is the net heat flux on the inlet surface of pore with the uniform and the non-uniform distribution. The first-order upwind scheme with SIMPLE algorithm is used for solving the governing equations.

**Table 3.4:** Boundary conditions for the steady-state heat transfer analysis.

Location	Uniform heat flux	Non-uniform heat flux
Inlet surface of absorber material $\left\{ q''_{net}\left(r\right)\big|_{z=0}\right\}$	$-\Sigma\sigma(T^4\left(r\right)\big|_{z=0} - T^4_{atm})$	$q''_s\big|_{z=0} - \Sigma\sigma(T^4\left(r\right)\big|_{z=0} - T^4_{atm})$
Outlet surface of absorber material	$q''_s\big|_{z=L}\left(r\right) = 0$	

Inlet to pore	$T_o = 300K$, $p_1 = 15.8Pa$ (gage total pressure)	
Outlet of pore	$p_2\big|_{z=L} = 0$ (gage static pressure)	
Circumferential area of the absorber material	$I(z) = $ Constant	$I(z) = \dfrac{q_s''(d_{pore})\sqrt{\varepsilon}\,\xi}{4(1-e^{-\xi L})}e^{-\xi z}$

For validation of the developed axis-symmetry based two-dimensional numerical approach, $100 \leq \dot{q}/\dot{m}_a$ (kJ/kg) ≤ 260 is considered as in the experiment by Sharma *et al.* (2015a). As an example, absorbers with the heating elements and the calibrated K-type thermocouples during an experiment are shown in Figure 3.4(b). Here, the applied power on the circumference of absorber ($\dot{q}_t$) is transferred to the primary air inside the pore ($\dot{q}_{pr}$) and to the return air around the absorber ($\dot{q}_r$) i.e.

$$\dot{q}_t = \dot{q}_{pr} + \dot{q}_r \quad . \tag{3.10}$$

However, in the developed model, only the primary air is considered and thus the transferred power $\dot{q}_{pr}$ to the same is recalculated from measurement. Because of the demonstrated volumetric heating in experiments, a uniform heat flux is applied on the circumference of absorber material for validation. No heat flux is imposed on the inlet surface of absorber material, see Table 4. A comparison between the measured and the computed steady-state air temperature at the pore outlet (T_{out}) shows an acceptable predictive capability of the numerical model with an uncertainty of ca. ±5%, see Figure 3.4(a). This is well within the reported experimental range. Thus, it is concluded that the adopted two-dimensional approach is reasonable for analyzing at least the current scenario. However, an analysis including the three-dimensional approach is also presented in the next sub-section.
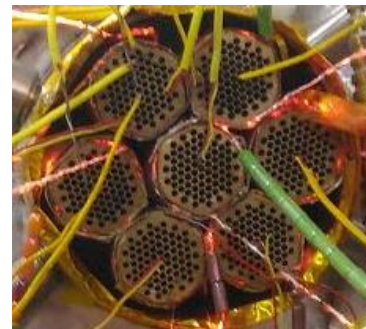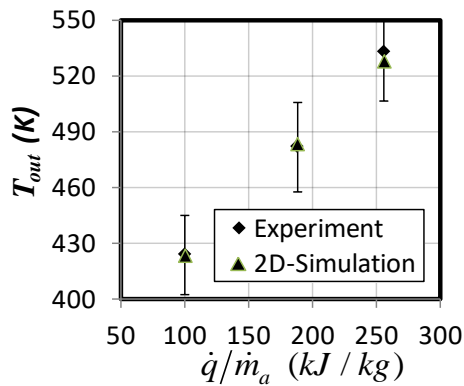
(a)   (b)

Figure 3.4: (a) A comparison between experiment and numerical analyzed air temperature at the absorber outlet; (b) absorbers with heating element during an experiment.

3.2.1.4 Results
In the two-dimensional simulation, a total pressure of 15.8 Pa corresponding to $\dot{q}/\dot{m}_a \sim$ 200 kJ/kg for a power ($\dot{q}$) of 1.03 W is employed as the inlet boundary condition. Zero gage pressure is applied at the outlet. The use of total inlet pressure simulates an operating condition in which all channels are exposed to the same suction. Therefore, the same pressure-drop is maintained even for the simulated partially blocked pore. Thus the flow inside a clean and a partly blocked pore is driven by the same pressure-drop as in a real absorber. The resulting Re_p

is about 175, 70 and 19 for the clean and partly blocked pores with uniform dust layer thickness of 100 μm ($\varepsilon \sim 42\%$) and 200 μm ($\varepsilon \sim 33\%$), respectively. The lower value of Re_p is a manifestation of the offered higher resistance to the flow by the blocked pore in comparison to the considered clean pore. Thus, the flow and thermal development length (~0.06 Re_p with $Pr \sim$ 0.7) will be shorter in the partly blocked pore as compared to its clean counterpart. It is also revealed that the non-uniform heat flux distribution leads to a higher solid temperature at the front surface than the uniform heat flux distribution case. Such elevation in solid temperature will result in increment of the radiation based heat loss. Moreover, the increment in solid temperature may lead to the deterioration of absorber material.
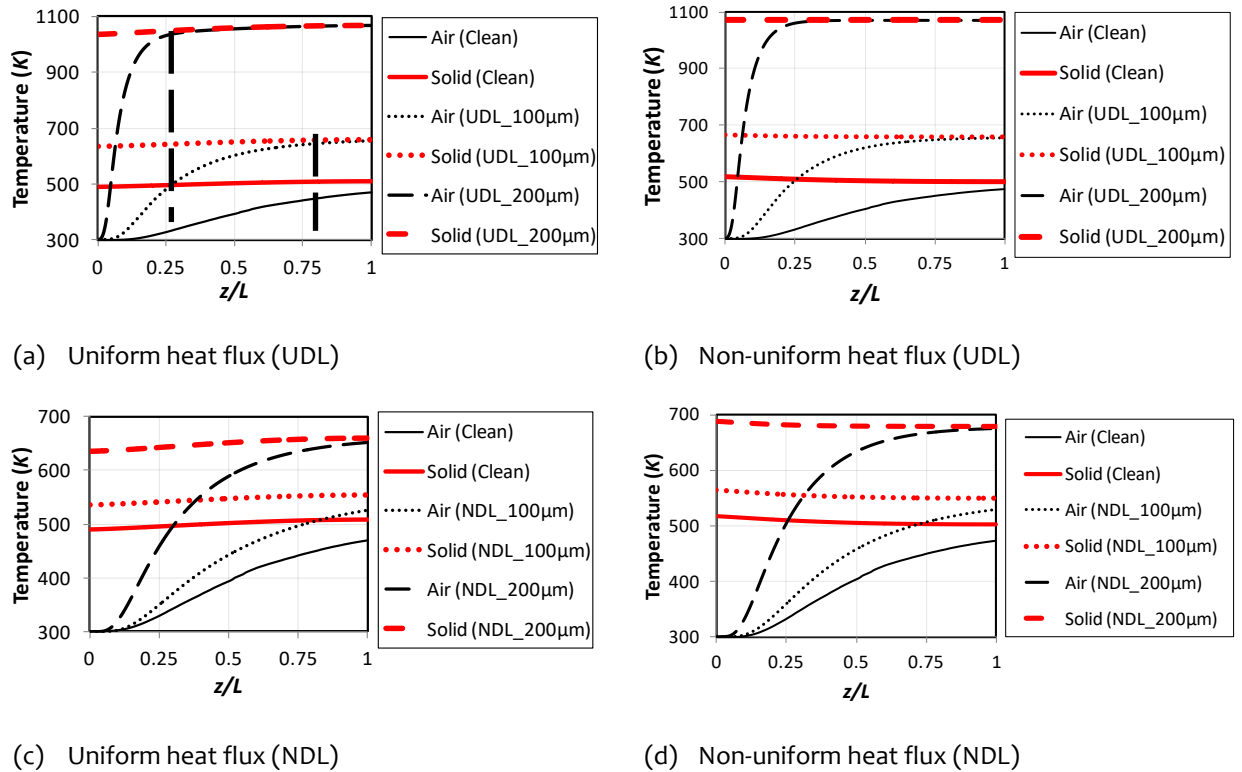

(a) Uniform heat flux (UDL)

(b) Non-uniform heat flux (UDL)

(c) Uniform heat flux (NDL)

(d) Non-uniform heat flux (NDL)

Figure 3.5: Axial temperature profile of fluid and solid with uniform dust layer thickness (UDL) and with non-uniform dust layer thickness (NDL) in an OVAR with circular straight channels.

The simulations are performed with a single clean and a partly blocked straight channel. The axial temperature variation of fluid and absorber material is shown in Figure 3.5 for the considered straight channels with the uniform and the non-uniform heat flux distributions. The deposition of dust on the channel surface will increase both flow and thermal resistance leading to an elevated air and absorber material temperature. This can be easily inferred from the decreasing Re_p with increasing thickness of uniform dust layer for the same applied pressure-drop. Therefore, a higher pressure-drop is required to maintain the same flow rate or Re_p in a partly blocked channel as in a clean channel. This is also evident from the analyses that show substantial rise in temperature with the partly blocked channel in comparison to its clean counterpart. The temperatures of solid and air increase with thickness of the dust layer, as expected. The modeled single circular channel with the applied UDL shows a temperature rise of about 150 K and 580 K with a dust layer thickness of 100 μm and 200 μm, respectively. Whereas with NDL a rise of about 40 K and 150 K with the deposited dust layers. This is attributed to the decreasing mass-flux for the same pressure-drop, which is confirmed by a shorter thermal development length, depicted by dotted vertical lines in Figure 3.5(a).

The numerically analyzed solid and fluid temperature contours for a clean and a partly blocked pore is shown in Figure 3.6. The scale is preserved for a better visual comparison.

Figure 3.5(a) shows that the fluid attains the solid temperature closer to the inlet for the blocked pore case in comparison to that of the clean pore. Thus, it may be inferred that the absorber solid will be exposed to a high temperature over a wider length with the blocked pore in comparison to the clean pore under a given operating condition. Thus, the need of in-situ cleaning is a must for mitigating the failure of such a system in arid deserts
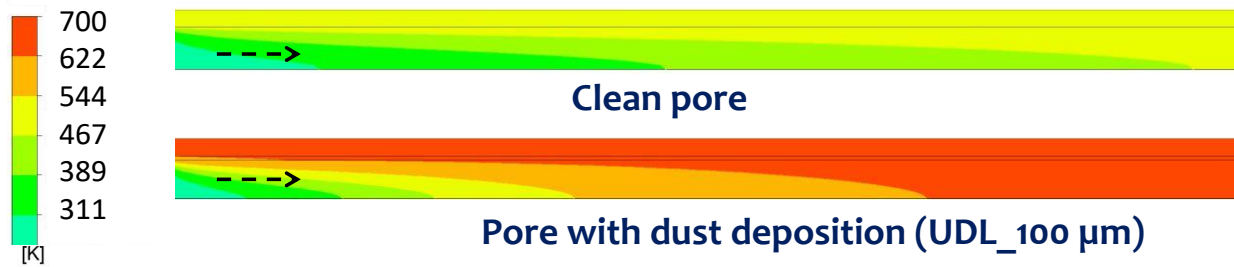

Figure 3.6: Temperature contours for a clean pore and for a partly blocked pore with uniform dust layer (UDL) thickness of 100 μm and the applied uniform heat flux along the pore length.

.

3.2.2 Three-dimensional Model: Square Straight Channel

In the previous section, the circular absorber pores are analyzed for the effect of dust deposition on the heat transfer in an absorber pore. The same is valid for the current receiver design of IIT Jodhpur. Some of the popular straight pore absorber based receivers contain square straight channels viz. HiTRec I/II and SolAir 200/3000. The analysis for the effect of dust deposition in the square channels is also performed. However, as in the case of circular pore, the axi-symmetric approach for the analysis is not applicable for the square straight channels. Hence, to analyze the effect of dust deposition on these absorbers, the three-dimensional simulations are performed, which is presented subsequently:

3.2.2.1 CFD analysis

For three-dimensional simulations, a square straight channel is selected from Luque *et al.* (2017), see Figure 3.7(a). The modeled clean straight square channel for the numerical investigation of heat transfer is shown in Figure 3.7(b). Simulations are also conducted in order to assess the effect of dust deposition on the heat transfer as illustrated in Figure 3.7(c). The generated mesh for a uniformly deposited dust layer in a pore is shown in Figure 3.7(d). The aim was to extend the presented analysis to a geometrically similar configuration of SolAir 200 absorber. The uniform heat flux boundary condition was employed on the circumference of clean and partly blocked pore as depicted in Figure 3.7(b) and (c). In this case, an input power of 6 W and a gage inlet pressure of 151 Pa leads to $\dot{q}/\dot{m}_a$ of 200 kJ/kg in a clean channel. For both the clean and partly blocked absorber channels, zero gage pressure is applied at the outlet. Also, the radiation based heat loss is incorporated at the front side of the channel using the user-defined functions. In the analysis a uniform dust layer thickness of 100 μm is considered and the numerical setup is summarized in Table 3.5.

Table 3.5: Setup for the three-dimensional analysis of a square straight channel.

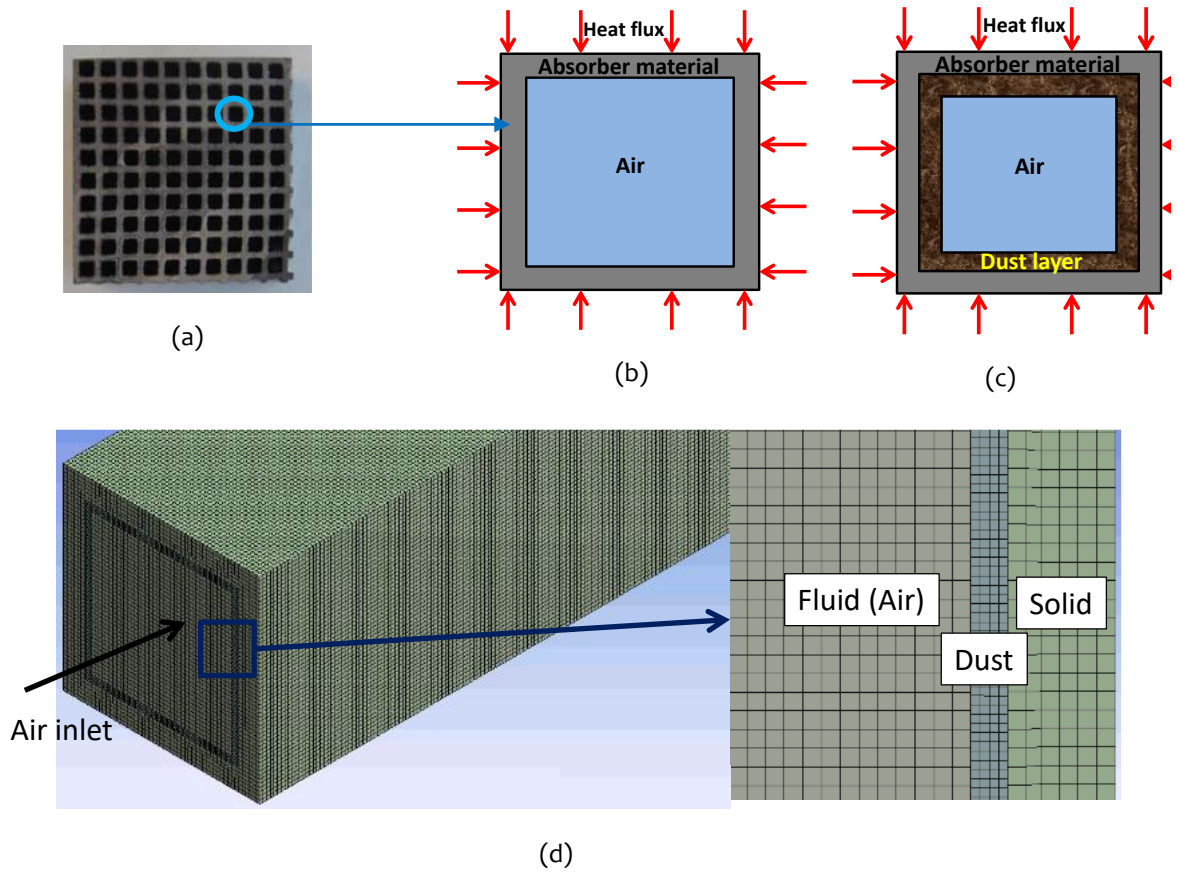| Mesh-type	Mesh-size (mm)	Mesh-quality	Governing Equations	Numerical Scheme	Convergence
Structured	0.025-0.05	Orthogonal quality: 0.98-0.99 Aspect Ratio: 1.92-2.15	Continuity, Momentum, Energy	First-order Upwind with SIMPLE algorithm	10^{-5}-10^{-6}

Figure 3.7: (a) The reference square absorber [Luque *et al.*, 2017]. The schematic depicting (b) clean and (c) dust deposited single straight channel, and (d) generated mesh for the partly blocked pore.

3.2.2.2 Results

The comparative assessment between clean and partly blocked square straight channel is given in Figure 3.8, where a temperature difference of about 120 K is observed. This demonstrates the increased resistance to heat transfer from solid to air in the partly blocked channels, and the fact that dust deposition may thus limit the operating temperature of OVARs. The temperature rise in circular and square shaped channels with the uniform dust layer thickness of 100 μm is quite comparable at the same power per unit mass flow rate. Thus it is concluded that the effects of dust deposition are very similar in these geometrically different flow channels. In the simulations, Reynolds number is about 780 and 500 for the clean and partly blocked square channels. The approximate thermal development lengths are 85 and 50 mm with the clean and partially blocked channels, respectively. Therefore, it is concluded that the effect of dust deposition remains, practically unaffected for a given $\dot{q}/\dot{m}_a$, with the different channel geometries and for the developing or developed flow conditions. The fact that partially-blocked absorbers operate at higher temperatures is detrimental in terms of thermal radiation losses (proportional to the fourth power of temperature), which will lower the thermal conversion efficiency of the OVAR in the event of dust storms.
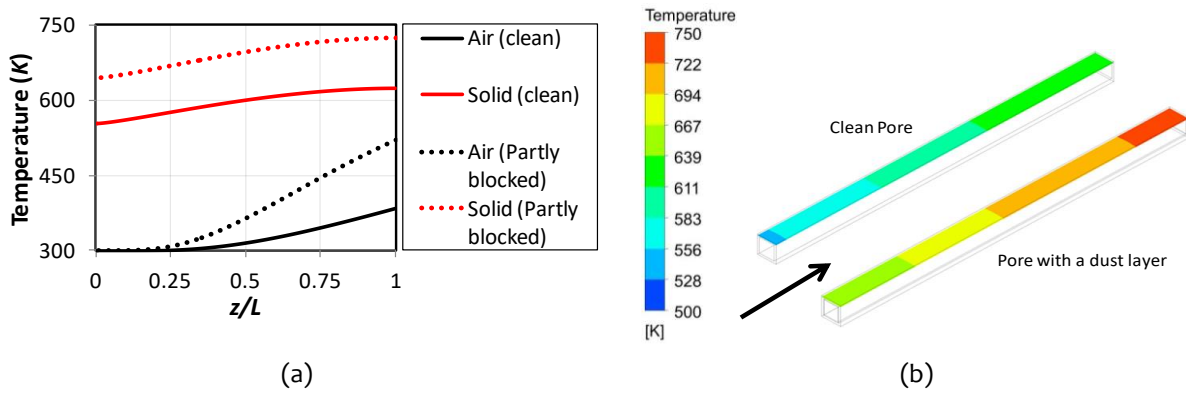
Figure 3.8: (a) Axial temperature profile along the centerline of absorber solid and fluid with UDL and a uniform heat flux distribution with reference square absorber [Luque *et al.*, 2017] and (b) Variation of solid temperature along the longitudinal direction a clean and partly blocked channel at the central plane.

3.3 SUMMARY

This chapter presents the detrimental effect of dust deposition and heat flux distribution in an absorber pore of an OVAR. The two-dimensional analysis with a dust-layer thickness of 100 μm (200 μm) on a circular straight pore and at a low $\dot{q}/\dot{m}_a = 200$ kJ/kg reveals a temperature rise of about 150 K (580 K) in comparison to a clean pore for both the uniform and the non-uniform heat flux distributions. The three-dimensional analysis for a square straight channel with dust layer of 100 μm also reveals a temperature increment of about 120 K for $\dot{q}/\dot{m}_a = 200$ kJ/kg. The application of uniform and non-uniform heat flux distribution also affirmed that the latter case leads to an elevation in temperature at the front side of the absorber. This will increase the radiation based heat loss and even result in failure of the absorber while operating at a high temperature. The dust deposition and a non-uniform heat flux distribution lead to an elevated temperature of the absorber and thus, these are detrimental for the operation of an OVAR. This will affect the installation of such a receiver in desert regions and thus, the need of an in-situ cleaning device is concluded. This is discussed in the next chapter.

…